

Correction of microwave pulse reflection by digital filters in superconducting quantum circuits

Liang-Liang Guo(郭亮亮), Peng Duan(段鹏), Lei Du(杜磊), Hai-Feng Zhang(张海峰), Hao-Ran Tao(陶浩然), Yong Chen(陈勇), Xiao-Yan Yang(杨小燕), Chi Zhang(张驰), Zhi-Long Jia(贾志龙), Wei-Cheng Kong(孔伟成), Zhao-Yun Chen(陈昭昀), and Guo-Ping Guo(郭国平)

Citation: Chin. Phys. B, 2024, 33 (**9**): 090303. DOI: 10.1088/1674-1056/ad5d98
Journal homepage: http://cpb.iphy.ac.cn; http://iopscience.iop.org/cpb

What follows is a list of articles you may be interested in

Interplay between topology and localization on superconducting circuits

Xin Guan(关欣), Bingyan Huo(霍炳燕), and Gang Chen(陈刚)
Chin. Phys. B, 2024, 33 (**6**): 060311. DOI: 10.1088/1674-1056/ad342c

Fast and perfect state transfer in superconducting circuit with tunable coupler

Chi Zhang(张驰), Tian-Le Wang(王天乐), Ze-An Zhao(赵泽安), Xiao-Yan Yang(杨小燕), Liang-Liang Guo(郭亮亮), Zhi-Long Jia(贾志龙), Peng Duan(段鹏), and Guo-Ping Guo(郭国平)
Chin. Phys. B, 2023, 32 (**11**): 110305. DOI: 10.1088/1674-1056/acf496

Blind quantum computation with a client performing different single-qubit gates

Guang-Yang Wu(吴光阳), Zhen Yang(杨振), Yu-Zhan Yan(严玉瞻), Yuan-Mao Luo(罗元茂), Ming-Qiang Bai(柏明强), and Zhi-Wen Mo(莫智文)
Chin. Phys. B, 2023, 32 (**11**): 110302. DOI: 10.1088/1674-1056/ace15a

Fabrication and characterization of superconducting multiqubit device with niobium base layer

Feifan Su(宿非凡), Zhaohua Yang(杨钊华), Shoukuan Zhao(赵寿宽), Haisheng Yan(严海生), Ziting Wang(王子婷), Xiaohui Song(宋小会), Ye Tian(田野), and Shiping Zhao(赵士平)
Chin. Phys. B, 2021, 30 (**10**): 100304. DOI: 10.1088/1674-1056/ac11d7

Universal quantum control based on parametric modulation in superconducting circuits

Dan-Yu Li(李丹宇), Ji Chu(储继), Wen Zheng(郑文), Dong Lan(兰栋), Jie Zhao(赵杰), Shao-Xiong Li(李邵雄), Xin-Sheng Tan(谭新生), and Yang Yu(于扬)
Chin. Phys. B, 2021, 30 (**7**): 070308. DOI: 10.1088/1674-1056/ac01c3

SPECIAL TOPIC — Quantum computing and quantum sensing

Correction of microwave pulse reflection by digital filters in superconducting quantum circuits

Liang-Liang Guo(郭亮亮)[1,2], Peng Duan(段鹏)[1,2,†], Lei Du(杜磊)[1,2], Hai-Feng Zhang(张海峰)[1,2], Hao-Ran Tao(陶浩然)[1,2], Yong Chen(陈勇)[1,2], Xiao-Yan Yang(杨小燕)[1,2], Chi Zhang(张驰)[3], Zhi-Long Jia(贾志龙)[3], Wei-Cheng Kong(孔伟成)[3], Zhao-Yun Chen(陈昭昀)[4], and Guo-Ping Guo(郭国平)[1,2,3,‡]

[1] *CAS Key Laboratory of Quantum Information, University of Science and Technology of China, Hefei* 230026, *China*
[2] *CAS Center for Excellence and Synergetic Innovation Center in Quantum Information and Quantum Physics, University of Science and Technology of China, Hefei* 230026, *China*
[3] *Origin Quantum Computing Company Limited, Hefei* 230088, *China*
[4] *Institute of Artificial Intelligence, Hefei Comprehensive National Science Center, Hefei* 230088, *China*

(Received 28 May 2024; revised manuscript received 25 June 2024; accepted manuscript online 2 July 2024)

Reducing the control error is vital for high-fidelity digital and analog quantum operations. In superconducting circuits, one disagreeable error arises from the reflection of microwave signals due to impedance mismatch in the control chain. Here, we demonstrate a reflection cancelation method when considering that there are two reflection nodes on the control line. We propose to generate the pre-distortion pulse by passing the envelopes of the microwave signal through digital filters, which enables real-time reflection correction when integrated into the field-programmable gate array (FPGA). We achieve a reduction of single-qubit gate infidelity from 0.67% to 0.11% after eliminating microwave reflection. Real-time correction of microwave reflection paves the way for precise control and manipulation of the qubit state and would ultimately enhance the performance of algorithms and simulations executed on quantum processors.

Keywords: reflection cancelation, digital filter, single-qubit gate, superconducting circuit

PACS: 03.67.Lx, 03.67.–a **DOI:** 10.1088/1674-1056/ad5d98

1. Introduction

Superconducting quantum circuit is one of the most promising platforms to achieve a quantum advantage with practical hardware.[1–3] In superconducting quantum computation, microwave pulses are often used to implement single-qubit gate[4,5] and two-qubit cross-resonance gate for fixed-frequency qubits.[6–8] Device fabrication and package processes have become more complex because of the increase in the qubit number and quantum processor size, which has led to a growing problem with the integrity of microwave signals.[9,10] For example, new multilayer interconnection techniques, such as through-silicon vias,[11–14] will increase the possibility of impedance mismatch, which causes the microwave reflection problem and decreases the fidelity of the quantum gates.[15,16] Therefore, it is crucial to characterize and compensate for the reflection by pre-distorting the desired pulses.

Pulse distortions have been well studied for superconducting qubits, but are mostly aimed at the baseband pulse transmitted on the fast flux line.[17–19] Because not only the amplitude but also the phase need to be considered, there is still a lack of a compatible reflection calibration method for microwave pulses on the drive line. An earlier work has determined a way to reduce quadrature (Q) distortions but leave the in-phase (I) response of the microwave signal uncompensated.[15] In that work, the conventional deconvolution method was employed to correct the pulse distortion, which requires determination of the complete pulse sequences in advance and is therefore incompatible with feedback-based control.

In this paper, we focus on eliminating unwanted microwave reflection using digital filters. This is because quantum instruction set architecture[20] and feedback-based control[21,22] require real-time correction of distortion, which can be achieved by integrating digital filters into the field-programmable gate array (FPGA). The real-time correction characteristic of the digital filter is a significant improvement over offline processing nature of deconvolution method. We pass the envelopes of the I–Q components of a microwave signal through digital filters to make the microwave signal appended with its modulated delay copy (MDC). This pulse can be used as a pre-distorted input to cancel out the reflection. We use the differential evolution optimization algorithm to determine the optimal digital filter coefficients and finally reduce the single-qubit gate error by about 80% to reach an average fidelity approaching 0.999. The reflection cancelation technique is not restricted to microwave-driven superconducting

†Corresponding author. E-mail: pengduan@ustc.edu.cn
‡Corresponding author. E-mail: gpguo@ustc.edu.cn

© 2024 Chinese Physical Society and IOP Publishing Ltd

qubits and is in principle applicable to any quantum computing platform manipulated at other frequency ranges.

2. Generation of the modulated delay copy of a microwave signal based on FIR filters

A digital filter in general can be represented by a linear constant coefficient difference equation of the form[23]

$$y(n) = \sum_{m=0}^{M} b_m x(n-m) - \sum_{k=1}^{N} a_k y(n-k), \tag{1}$$

where $y(n)$ is the output in time and $x(n)$ is the input. The variable n is integer-valued and represents discrete instances in time. n can be transformed into the continuous-time variable t using the relationship $t = nT_s$, where T_s is the sampling interval. Equation (1) describes a recursive approach for computing the current output, given the input values and previously computed output values. m going from 0 to M refers to the indexes of present and past inputs, while k going from 1 to N refers to the indexes of past outputs. b_m and a_k are called the filter tap coefficients.

If the second term on the right-hand side of Eq. (1) is not zero, then we are talking about infinite impulse response (IIR) filters. Otherwise, Eq. (1) becomes a finite impulse response (FIR) filter

$$y(n) = \sum_{m=0}^{M} b_m x(n-m). \tag{2}$$

FIR filters delay and correct a sequence using only the input signal without considering the output. In other words, they perform a feed-forward operation. On the other hand, an IIR filter modifies the signal with dependence on both the input and output, meaning that it also performs feedback. Therefore, M and N in Eq. (1) are called the feedforward and feedback filter orders, respectively. In Fig. 1(a), we illustrate how an FIR filter works. The signal values $x(n)$ are delayed by a single time step at each z^{-1} block, multiplied by the tap coefficients b_m, and summed together to produce the filtered signal output values $y(n)$.

If we set the filter tap coefficients other than b_{n_d} to zero, we have $y(n) = b_{n_d} x(n-n_d)$ and n_d is a positive integer. This FIR filter delays a signal by an integer number of time steps. In the continuous-time domain, the input and output of the FIR filter satisfy $y(t) = b_{n_d} x(t-t_d)$, where $t_d = n_d T_s$.

Microwave signals are always used to excite qubits in solid state quantum computation.[9] Here, we intend to adjust the amplitude and phase of a microwave signal while creating a delay. We design a digital module to generate such a modulated delay copy of the microwave signal, which can be seen in Fig. 1(b). An arbitrary microwave signal $s(t)$ with an angular frequency of ω can be decomposed into in-phase and quadrature-phase components as

$$s(t) = v_I(t)\cos(\omega t) + v_Q(t)\sin(\omega t), \tag{3}$$

where $v_I(t)$ and $v_Q(t)$ are envelopes of the I–Q components. There are four FIR filters in the digital module, which are shown as green blocks in Fig. 1(b). The envelopes are digitally mixed with a continuously running numerically controlled oscillator (NCO)[24,25] after passing through the FIR filters to generate the output $O(t)$. We denote the tap coefficients of each FIR filter as b_m^i and $i = 1, 2, 3, 4$. If we set all the tap coefficients to zero except for

$$\begin{aligned} b^1_{n_d} &= A\cos\varphi, \quad b^2_{n_d} = A\sin\varphi, \\ b^3_{n_d} &= -A\sin\varphi, \quad b^4_{n_d} = A\cos\varphi, \end{aligned} \tag{4}$$

the output of the digital module is

$$\begin{aligned} O(t) &= [b^1_{n_d} v_I(t-t_d) + b^2_{n_d} v_Q(t-t_d)]\cos(\omega t) \\ &\quad + [b^3_{n_d} v_I(t-t_d) + b^4_{n_d} v_Q(t-t_d)]\sin(\omega t) \\ &= v_I(t-t_d)[\cos(\omega t) b^1_{n_d} + \sin(\omega t) b^3_{n_d}] \\ &\quad + v_Q(t-t_d)[\cos(\omega t) b^2_{n_d} + \sin(\omega t) b^4_{n_d}] \\ &= A v_I(t-t_d)\cos(\omega t + \varphi) + A v_Q(t-t_d)\sin(\omega t + \varphi). \end{aligned} \tag{5}$$

Therefore, the FIR-filter-based digital module delays $s(t)$ by a time t_d and adds a relative amplitude A and phase φ to that pulse. If we want to keep the output $O(t)$ to be $s(t)$, we can set all the tap coefficients to zero other than

$$b^1_0 = 1, \quad b^4_0 = 1. \tag{6}$$

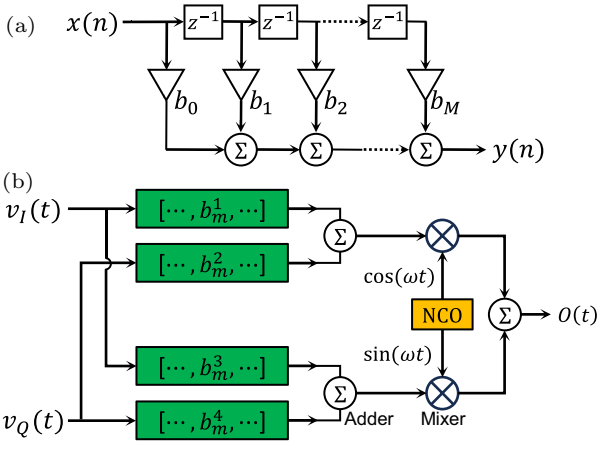


Fig. 1. (a) Schematic diagram of the FIR filter. The input signal $x(n)$ is delayed by a time step at each z^{-1} block and summed together after multiplying the tap coefficient b_m to obtain the output signal $y(n)$. (b) A digital module we designed to generate a modulated delay copy of the microwave signal. The green blocks represent FIR filters with tap coefficients b_m^i and the NCO is used to generate sine and cosine signals that are orthogonal to each other. This module takes the envelopes of the I–Q components of a microwave signal as input and introduces a delay time t_d, relative amplitude A and phase φ to the microwave signal when the filter coefficients satisfy Eq. (4).

3. Microwave pulse reflection in superconducting quantum circuits

Experiments are carried out on the frequency-tunable transmon qubit,[26,27] for which microwave pulses are usually used to implement single-qubit gates. As illustrated in Fig. 2(a), microwave pulses are generated based on the double-frequency conversion scheme in our setup, which includes two separate mixing stages fed by two different local oscillator (LO) signals.[28] Modulated intermediate-frequency (IF) signals at approximately 1 GHz, digitally defined using a digital-to-analog converter (DAC), are mixed twice sequentially to be upconverted to the frequency range of 3.75 GHz–8.25 GHz (see Appendix A for more details of the mixing module). Quantum device parameters and experimental wiring setup can be found in Appendix B.

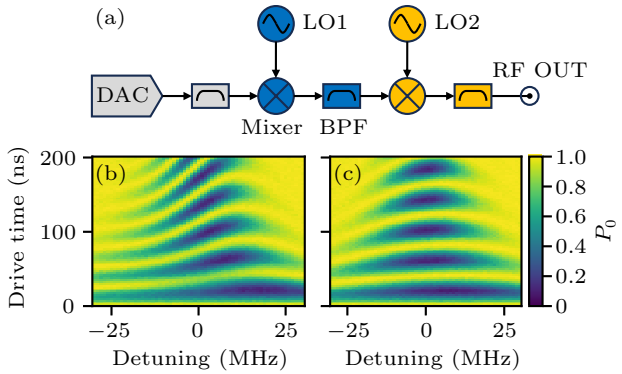


Fig. 2. Frequency up-conversion scheme and Rabi oscillations of the qubit as a function of drive time and drive detuning. (a) Diagram of the double-frequency conversion scheme used to upconvert the IF signals with a frequency of f_{IF} to radio frequency (RF) signals at 3.75 GHz–8.25 GHz. We can simply regard the mixing process as a frequency translation operation, and the output frequency f_{RF} of the mixing module is $f_{\mathrm{IF}}+(f_{\mathrm{LO2}}-f_{\mathrm{LO1}})$, where f_{LO1} and f_{LO2} are the frequencies of the two LO signals. The sampling rate of the DAC is 3.2 GSa/s, and the band-pass filter (BPF) at each stage is used to eliminate spurious signals and unwanted sideband. [(b) and (c)] Rabi oscillation without and with reflection cancelation. The Rabi pulse is shaped with a raised-cosine envelope and is driven at an amplitude corresponding to the 25-MHz oscillation when no drive detuning. When we use FIR filters to compensate for the reflection, the Rabi oscillation of the qubit recovers to the regular Chevron pattern.

When the generated microwave signals are resonant with the qubit transition, Rabi oscillations occur. Figure 2(b) shows the change in the probability P_0 that the qubit is in the ground state as we scan the drive time and the detuning between the drive frequency and qubit frequency. The strongly distorted Chevron pattern indicates that the microwave pulses are distorted when transmitting through the drive line. Specifically, we can reproduce a similar pattern in numerical simulation, which can be seen in Appendix C, by considering only drive pulse distortion due to reflections.

In Fig. 3(a), we illustrate the reflection and transmission of a microwave pulse when two reflection nodes are present in the signal transmission chain. The input pulse bounces back and forth between these two nodes and hits the qubit multiple times at a time interval t_i, as shown in Fig. 3(b). We denote the successive pulses that arrive at the qubit as the s-th-order reflection of the input signal. The premier pulse that reaches the qubit first is represented by $s=0$. The reflected pulse of each order experiences one additional round trip between the two nodes compared with the previously reached pulse, thus accumulating an extra complex reflection coefficient $\Gamma e^{j\Delta\varphi}$. If t_i is shorter than the width of the input pulse, the reflected pulse will overlap with the premier pulse, resulting in complex dynamics such as a distorted Rabi pattern.

We can eliminate the reflection by setting the intended pulse appended with its MDC as the input signal, as illustrated in Fig. 3(c). This pre-distortion pulse can be achieved by integrating the digital module in Fig. 1(b) into the DAC and setting the FIR filters coefficients combining Eqs. (4) and (6). In this way, the output of the DAC is a modulated IF signal appended with its MDC. Because the double-frequency conversion only shifts the frequency of the IF signal while preserving every other characteristic, the final output of the mixing module in Fig. 2(a) is our wanted pre-distortion pulse at frequency f_{RF}.

When the parameters for generating the FIR filters match $t_{\mathrm{d}}=t_i$, $A=\Gamma$, $\varphi=\Delta\varphi+\pi$, the 0-th-order reflection of the MDC can cancel out the first-order reflection of the intended pulse. Furthermore, the first-order reflection of the MDC is multiplied by $\Gamma e^{j\Delta\varphi}$ relative to the 0-th-order reflection of the MDC, while the second-order reflection of the intended pulse is identically scaled relative to its first-order reflection. Therefore, the first-order reflection of the MDC counteracts the second-order reflection of the intended pulse. In general, the s-th-order reflection of the MDC cancels out the $(s+1)$-th-order reflection of the intended pulse. Consequently, as depicted in Fig. 3(c), when we use the ideal pulse appended with its MDC with appropriate parameters for the pre-distortion input, the qubit receives the desired signal without reflected pulses.

4. Experimental results

Next, we experimentally determine the three parameters of the appended MDC to mitigate the reflections. First, we use the pulse sequence shown in Fig. 3(d) to identify each order of reflection and extract the reflection delay t_i. On the XY control line, we play a X_π gate with a fixed delay of 100 ns. The X_π gate corresponds to a rotation of 180° around the x-axis on the Bloch sphere and is shaped with a raised-cosine envelope. To avoid overlap between the reflections, we should choose as fast a single-qubit gate as possible in this experiment, which we use here is 10 ns. On the Z control line, we apply a square pulse with a width of 60 ns and amplitude to shift the qubit frequency by approximately 100 MHz from the working point. We scan the delay Δt of the square pulse and measure the probability P_1 when the qubit is in the excited state. As Δt exceeds

40 ns, the square wave successively shifts the qubit frequency at each reflection away, causing the reflected pulse of the corresponding order to no longer excite the qubit. Furthermore, when the square pulse covers all orders of reflection, the qubit cannot be excited at all.

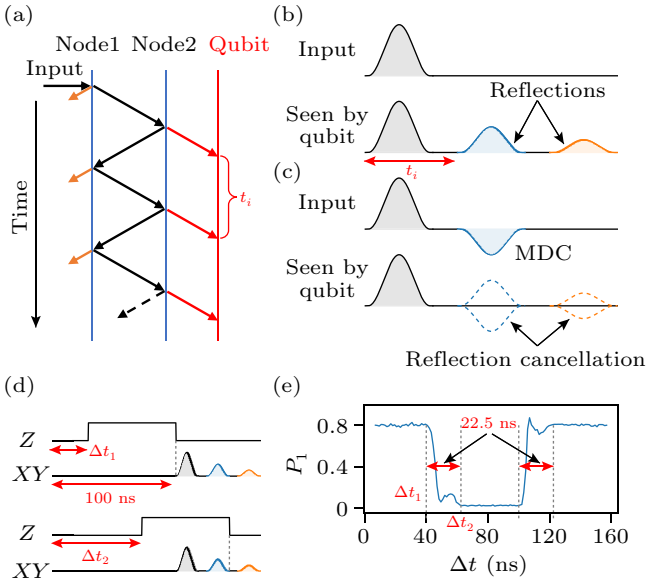


Fig. 3. (a) Schematic diagram of signal transmission and reflection when there are two reflection nodes on the control line. An input microwave pulse can hit the qubit multiple times at a time interval t_i. Suspicions regarding the potential locations of these two reflection nodes are detailed in Appendix B. (b) Illustration of intended pulse we play into the input of the control line and the resulting pulse seen by qubit due to reflection. (c) We set intended pulse appended with its modulated delay copy as the pre-distortion input, and the qubit receives the desired pulse because the s-th-order reflection of the MDC cancels the $(s+1)$-th-order reflection of the intended pulse. (d) We scan the delay of the square pulse with a width of 60 ns on the Z control line to identify each order of reflection of the π pulse applied on the XY line. The change in the qubit excitation is shown in panel (e). We plot two special locations of the square pulse in panel (d) that correspond to the delays denoted as Δt_1 and Δt_2 in panel (e).

If there was no microwave reflection problem, the qubit would not be excited when Δt is within the range of 50 ns–100 ns. However, in the experimental results shown in Fig. 3(e), an additional excitation peak appears around $\Delta t = 55$ ns, which arises from the first-order reflection of the π pulse. The absence of more excitation peaks is likely because the amplitude of the reflection coefficient Γ is relatively small, which makes higher-order reflections very weak. We mark two values of Δt in Fig. 3(e), denoted as Δt_1 and Δt_2, which correspond to the different positions of the square pulse, as illustrated in Fig. 3(d). The difference between Δt_1 and Δt_2 is 22.5 ns, which is equal to the sum of t_i and the width of the single-qubit gate. Therefore, we can estimate that t_i is approximately 12.5 ns.

As Δt increases beyond 100 ns, the qubit frequency at each reflection is successively no longer influenced by the square pulse applied on the Z line, and the qubit can be re-excited. We can also extract t_i from the change in the population of qubit around $\Delta t = 100$ ns, which is also marked in Fig. 3(e).

Microwave reflection increases the control error of single-qubit operations.[15,16,29] We then optimize the three parameters of the appended MDC using the differential evolution (DE) algorithm after we obtain t_i,[30] so that the reflection can be canceled out and the single-qubit gate fidelity can be improved. Here, the single-qubit gate is implemented by the derivative removal by adiabatic gate (DRAG) method[4,31] with a 20 ns raised cosine envelope and a 2.5 ns pad. We use randomized benchmarking (RB) to characterize the performance of the single-qubit gates without reflection cancelation, and the result is shown in Fig. 4(b). The RB sequence is a sequence of randomly chosen Clifford gates with length m, appended by a recovery Clifford that makes the ideal operation the identity.[32,33] The qubit is prepared in $|0\rangle$ and we measure the survival probability of state $|0\rangle$ (the sequence fidelity) as m increases. For each fixed length m, we measure $k = 30$ different sequences. The error bar in Fig. 4(b) is the standard deviation of the fidelity of the k sequences. Due to the influence of reflection, the error rate of the single-qubit gates is relatively high, which is 0.67%, and the error bar is also large.

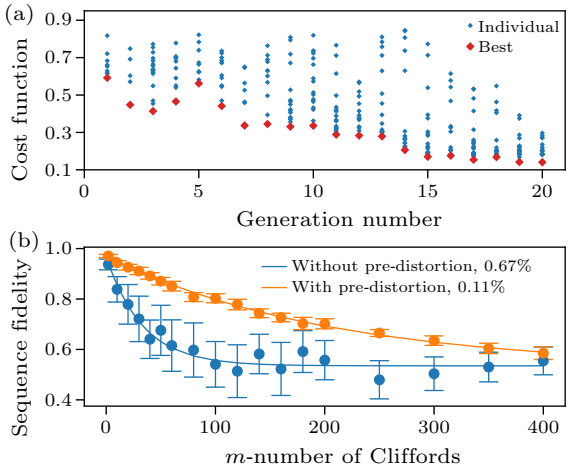


Fig. 4. (a) Evolution process of the DE algorithm as the generation number increases. The blue diamonds represent the values of the individual at each iteration of the population, and the red diamonds highlight the best individual of the population at each generation. (b) Comparison of single-qubit gate error with and without pre-distortion compensation for microwave reflection. The gate infidelity is extracted by a randomized benchmarking measurement. At each m, we measure $k = 30$ random sequences and fit the average value over the fidelity of these sequences by $f_{\text{ave},m} = Ap^m + B$, where state preparation and measurement errors are absorbed in parameters A and B. The average gate error is then calculated by $(1-p)/2/1.875$, where 1.875 is derived from the average physical gates contained in a Clifford gate.[34] The standard deviation of the fidelity of k random sequences is displayed as the error bar.

We denote the average value and standard deviation of the fidelity of the k different sequences as $f_{\text{ave},m}$ and $f_{\text{std},m}$ when the number of Cliffords is m. We want to improve the $f_{\text{ave},m}$ and decrease the $f_{\text{std},m}$ by DE optimization algorithm, so we define the cost function as $f(t_\text{d}, A, \varphi) = -f_{\text{ave},m} + f_{\text{std},m} + 1$ and set $m = 50$ here.[35] According to the results in Fig. 3(e), t_i is estimated to be approximately 12.5 ns and is set as the initial value of t_d. The population size of the DE algorithm is set to

20. For the initial values of A and φ, we take $A = 0.05$, 0.15, 0.25, and 0.35, and φ takes five values evenly within the range of 0 to 2π. The 20 parameter groups formed are taken as the initial population of the DE algorithm.

The iterative process of the DE algorithm is shown in Fig. 4(a). During each function evaluation, we automate the execution of a series of experiments,[36] including calibrating the parameters of single-qubit gates using routine experiments[4] and then calculating the cost function through the RB experiment. In some iterations, the generated pre-distorted waveforms actually make the pulses received by the qubit even worse, which causes the automated calibration of the single-qubit gates to fail. In such cases, we directly record the cost function as 1, which is not shown in Fig. 4(a), and proceed to the next function evaluation.

As can be seen from Fig. 4(a), after 20 generations of evolution, the DE algorithm converges to the optimal value, that is, $t_{\rm d} = 13.750$ ns, $A = 0.205$, $\varphi = 3.746$ rad. After obtaining the above parameters, we verify the effect of using FIR filters to implement the pre-distortion scheme shown in Fig. 3(c) to compensate for the microwave reflection. We recalibrate the parameters of the single-qubit gates and characterize their fidelity after reflection cancelation. The result is shown in Fig. 4(b) and the error of the single-qubit gates is reduced to 0.11%, which is an 80% reduction compared with the error of the single-qubit gates without reflection cancelation. In addition, the standard deviation of the fidelity of 30 random sequences is also significantly reduced. We also measure the Rabi oscillation after pre-distortion compensation for reflection, and the results are shown in Fig. 2(c). The Chevron pattern does not exhibit the obvious distortion, indicating that the use of FIR filters for microwave reflection cancelation is effective. Additional data from another qubit experiencing a similar reflection problem can be seen in Appendix D.

5. Conclusion

In conclusion, we have presented an approach for the characterization and cancelation of microwave reflection in qubit drives, which allowed us to reduce the average error per gate by about 80%. Starting from illustrating the resulting pulse seen by qubit when there are two reflection nodes on the drive line, we propose to mitigate the reflection problem by setting the intended pulse appended with its modulated delay copy as the pre-distortion input. We achieve the pre-distortion correction by passing the envelopes of I–Q components of the intended pulse through FIR filters. The digital pre-distortion module is now implemented and verified in software, and integrating the FIR filters and NCO into the FPGA to achieve real-time distortion correction is an ongoing work. We are still locating the two reflection nodes, and placing an isolator between the two nodes can also suppress the reflection problem. Our reflection mitigation technique improves the fidelity of quantum gates and may play a crucial role in quantum computation as the interconnection of control lines for qubits becomes increasingly complex.

Appendix A: Frequency up-conversion scheme based on double-frequency conversion

The conventional method for up-converting an intermediate frequency (IF) signal generated by a digital-to-analog converter (DAC) to a microwave signal resonant with the qubit is the IQ-mixing scheme. However, practical IQ mixers exhibit non-idealities, necessitating calibration of DC-offsets, relative amplitude and phase to mitigate unwanted local oscillator (LO) and image leakage. Moreover, the calibration parameters of the IQ mixer tend to drift over time and with temperature, thus requiring periodic recalibration, which significantly increases the complexity of the experimental procedures. In our experimental system, we employ an alternative frequency up-conversion technique based on double-frequency conversion, which obviates the need for IQ-calibration.

As can be seen in Fig. A1, we first generate an IF signal $S_0(f)$ with a frequency $f_{\rm IF}$ ranging from 0.8 GHz to 1.3 GHz using a DAC operating at a sampling rate of 3.2 GSa/s. This signal is then passed through a bandpass filter with an identical passband range to eliminate spurious signals.

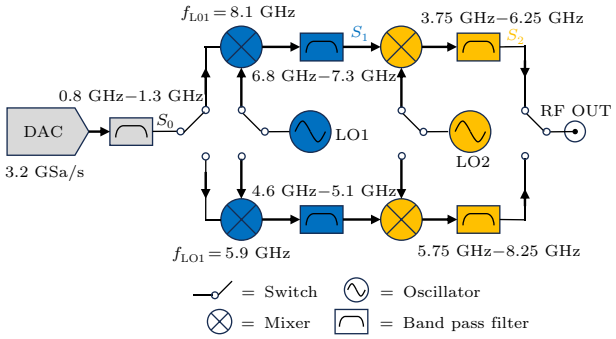


Fig. A1. Diagram of the mixing module used to generate microwave signals in the frequency range of 3.75 GHz–8.25 GHz. Switches can be switched to the corresponding path where the frequency of the LO1 is equal to 8.1 GHz or 5.9 GHz to produce output signals within the frequency range of 3.75 GHz–6.25 GHz or 5.75 GHz–8.25 GHz.

Next, $S_0(f)$ undergoes a first-stage frequency mixing with a fixed-frequency LO signal, LO1, which is continuously running at $f_{\rm LO1} = 5.9$ GHz or 8.1 GHz. Depending on whether $f_{\rm LO1}$ equals 5.9 GHz or 8.1 GHz, our mixing module bifurcates into two paths to produce output signals in different frequency bands.

We first illustrate the signal mixing and filtering process for the path where $f_{\rm LO1} = 8.1$ GHz. Upon mixing $S_0(f)$ with LO1, we obtain signals at frequencies $f_{\rm LO1} \pm f_{\rm IF}$. We employ an analog bandpass filter with a passband frequency of 6.8 GHz to 7.3 GHz to retain the sideband signal at frequency

$f_{\mathrm{LO1}} - f_{\mathrm{IF}}$, denoted as $S_1(f)$, while rejecting the emerging image component at the frequency $f_{\mathrm{LO1}} + f_{\mathrm{IF}}$. Subsequently, $S_1(f)$ undergoes a second-stage mixing with a frequency-tunable LO signal, LO2, whose frequency f_{LO2} spans from 10.85 GHz to 13.05 GHz. The resulting mixed signal contains both sum and difference frequency sidebands, which are filtered by a bandpass filter with a passband of 3.75 GHz to 6.25 GHz to retain the sideband signal at $f_{\mathrm{LO2}} - (f_{\mathrm{LO1}} - f_{\mathrm{IF}})$, denoted as $S_2(f)$. $S_2(f)$ is the ultimate microwave signal output from the path with $f_{\mathrm{LO1}} = 8.1$ GHz, which has a frequency range of 3.75 GHz to 6.25 GHz.

For the alternative path with $f_{\mathrm{LO1}} = 5.9$ GHz, the corresponding bandpass filter frequency ranges are marked in Fig. A1. Through this path, we obtain output signals within the frequency range of 5.75 GHz to 8.25 GHz. Based on the desired output frequency values and the IF frequency we set, the mixing module automatically switches to the appropriate path and sets f_{LO2} to generate microwave signals at the required frequencies.

Appendix B: Device information and experimental wiring setup

Our qubit is a frequency-tunable transmon structure, each equipped with two control lines. A microwave drive line is used to excite the qubits to execute single-qubit gates, and a flux control line is used to tune the qubit frequency to facilitate the implementation of two-qubit gates. The qubit is dispersively coupled to a resonator for state readout. Table B1 lists the key performance metrics of our superconducting quantum device, and Fig. B1 illustrates the experimental wiring setup.

The Z-control signal for the qubit is generated by an arbitrary waveform generator (AWG), which is capable of superimposing any arbitrary waveform onto a voltage bias. The methodology for generating the XY-control signals for the qubit is described in Appendix A. The readout signal is amplified at the mixing chamber (MC) stage using a near-quantum-limited impedance-matched parametric amplifier (IMPA).

We attenuate and filter the signal at different stages of the dilution refrigerator to reduce the noise incident on the qubits. For the XY control lines, we use a 20-dB attenuator at the 4 K stage and a 20-dB attenuator in series with a 6-GHz low-pass filter at the MC stage. In the MC stage, we have incorporated an additional wiring patch panel. Cables made of low-density polytetrafluoroethylene (PTFE) with a length of 50 cm are employed to connect from the low-pass filter to this patch panel, and subsequently from the patch panel to the SMP connectors mounted on the chip enclosure. Our quantum chip is wire-bonded to the printed circuit board (PCB) within the chip enclosure, and the distance is approximately 5 cm from the SMP connectors on the chip enclosure to the wire-bonding points.

Table B1. Overview of key parameters of our superconducting quantum device. The experimental data in the main text were collected from Q1 and the data in Appendix D were collected from Q2. $\omega_{\mathrm{Max}}/2\pi$ denotes the maximum frequency of the qubit. $\omega_{\mathrm{Idle}}/2\pi$ represents the idle frequency of the qubit. $\omega_{\mathrm{r}}/2\pi$ signifies the resonance frequency of the readout resonator. T_1 and T_2^* are the energy relaxation time and dephasing time, respectively, which are both measured at the idle frequency. $\eta/2\pi$ is the anharmonicity of the qubit at the idle frequency. f_{00} (f_{11}) is the probability of correctly identifying the qubit state when it is initially prepared in $|0\rangle$ ($|1\rangle$) state.

Parameter	Q1	Q2
$\omega_{\mathrm{Max}}/2\pi$ (GHz)	4.657	4.743
$\omega_{\mathrm{Idle}}/2\pi$ (GHz)	4.645	4.737
$\omega_{\mathrm{r}}/2\pi$ (GHz)	7.237	7.194
T_1 (μs)	17.8	13.5
T_2^* (μs)	9.4	6.2
$\eta/2\pi$ (MHz)	−201	−202
f_{00} (%)	97.8	96.9
f_{11} (%)	88.7	85.2

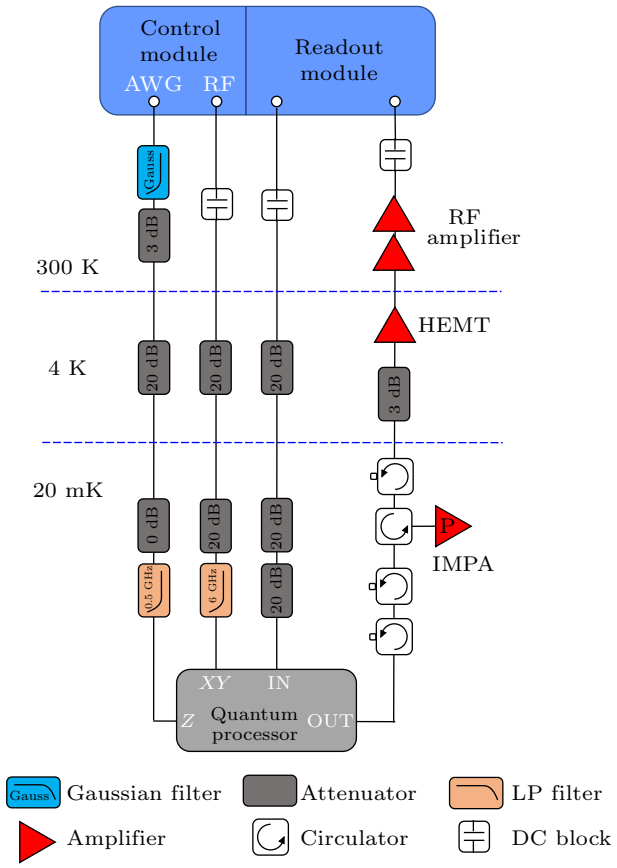


Fig. B1. Full wiring diagram of the experimental setup.

We suspect that the higher-than-usual reflections may stem from a loose connection at the joint between the 20-dB attenuator and the low-pass filter, as well as impedance deviations from the nominal 50 Ω in the wiring bonding lines. The approximate distance between these two locations is 105 cm. Furthermore, the additional latency introduced by the low-pass filter and various interconnectors could, when taken into account, seem to align with our measured reflection delay of 13.75 ns.

Appendix C: Simulation results of the Rabi pattern

We have found that the experimentally observed distorted Rabi oscillation patterns can be reproduced in simulations by accounting for the presence of reflected microwave pulses. The simulation results are depicted in Fig. C1 where the reflection parameters used for Fig. C1(a) are based on the results obtained from the reflection cancelation measurements.

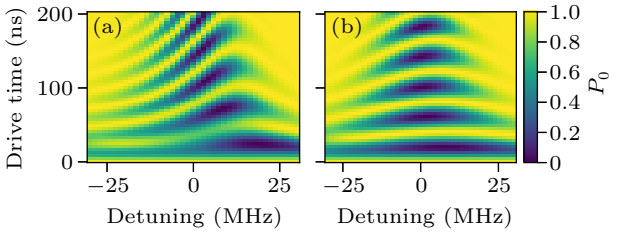


Fig. C1. Simulation results of Rabi oscillation with (a) and without (b) microwave reflection problem.

Appendix D: Additional data

We apply our compensation strategy to another qubit experiencing similar reflection issues to demonstrate the generality of the proposed compensation scheme for microwave control line reflections. The qubit information labeled Q2 is listed in Table B1. The parameter extraction procedure for the predistortion pulse and the resulting improvement of the single-qubit gate fidelity, which can be seen in Fig. D1, are similar to those detailed in the main text. The parameters we obtain are $t_{\rm d} = 15.625$ ns, $A = 0.279$, $\varphi = 2.045$ rad. The single-qubit gate infidelity is reduced from 0.73% to 0.12% after eliminating microwave reflection.

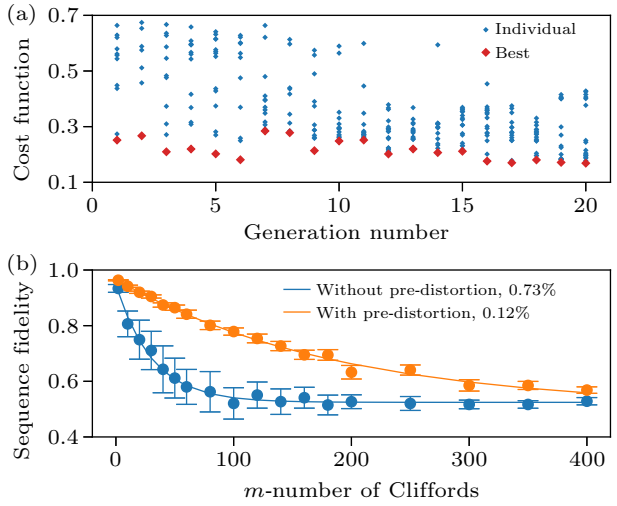


Fig. D1. Evolution process of the DE algorithm (a) and comparison of the single-qubit gate error with and without pre-distortion compensation for microwave reflection (b) for another test qubit labeled Q2.

Acknowledgments

Project supported by the National Natural Science Foundation of China (Grant Nos. 12034018 and 11625419). This work was partially carried out at the USTC Center for Micro and Nanoscale Research and Fabrication.

References

[1] Arute F, Arya K, Babbush R, *et al.* 2019 *Nature* **574** 505
[2] Wu Y, Bao W S, Cao S, *et al.* 2021 *Phys. Rev. Lett.* **127** 180501
[3] Zhu Q, Cao S, Chen F, *et al.* 2022 *Science Bulletin* **67** 240
[4] Chen Z, Kelly J, Quintana C, *et al.* 2016 *Phys. Rev. Lett.* **116** 020501
[5] McKay D C, Wood C J, Sheldon S, Chow J M and Gambetta J M 2017 *Phys. Rev. A* **96** 022330
[6] Chow J M, Córcoles A D, Gambetta J M, *et al.* 2011 *Phys. Rev. Lett.* **107** 080502
[7] Patterson A, Rahamim J, Tsunoda T, *et al.* 2019 *Phys. Rev. Appl.* **12** 064013
[8] Sundaresan N, Lauer I, Pritchett E, Magesan E, Jurcevic P and Gambetta J M 2020 *PRX Quantum* **1** 020318
[9] Bardin J C, Slichter D H and Reilly D J 2021 *IEEE Journal of Microwaves* **1** 403
[10] Rosenberg D, Weber S J, Conway D, *et al.* 2020 *IEEE Microwave Magazine* **21** 72
[11] Yost D R W, Schwartz M E, Mallek J, *et al.* 2020 *npj Quantum Information* **6** 59
[12] Vahidpour M, O'Brien W, Whyland J T, *et al.* 2017 arXiv: 1708.02226
[13] Alfaro-Barrantes J, Mastrangeli M, Thoen D, Visser S, Bueno J, Baselmans J and Sarro P M 2020 *IEEE Electron Device Lett.* **41** 1114
[14] Grigoras K, Yurttagül N, Kaikkonen J P, *et al.* 2022 *IEEE Transactions on Quantum Engineering* **3** 1
[15] Gustavsson S, Zwier O, Bylander J, Yan F, Yoshihara F, Nakamura Y, Orlando T P and Oliver W D 2013 *Phys. Rev. Lett.* **110** 040502
[16] Dogan E, Rosenstock D, Le Guevel L, *et al.* 2023 *Phys. Rev. Appl.* **20** 024011
[17] Rol M A, Ciorciaro L, Malinowski F K, *et al.* 2020 *Appl. Phys. Lett.* **116** 054001
[18] Foxen B, Mutus J, Lucero E, *et al.* 2018 *Superconductor Science and Technology* **32** 015012
[19] Zhang C, Wang T L, Guo L L, Yang X Y, Yang X X, Duan P, Jia Z L, Kong W C and Guo G P 2023 *Appl. Phys. Lett.* **122** 024001
[20] Butko A, Michelogiannakis G, Williams S, *et al.* 2020 *2020 International Conference on Rebooting Computing (ICRC),* December 1-3, 2020, Atlanta, GA, USA, p. 66
[21] Hu L, Ma Y, Cai W, *et al.* 2019 *Nat. Phys.* **15** 503
[22] Xiang L, Zong Z, Sun Z, Zhan Z, Fei Y, Dong Z, Run C, Jia Z, Duan P, Wu J, Yin Y and Guo G 2020 *Phys. Rev. Appl.* **14** 014099
[23] Ingle V K and Proakis J G 2012 *Digital Signal Processing Using MATLAB*, 3nd edn. (Stamford, Conn.: Cengage Learning) pp.212-239
[24] van Dijk J P G, Patra B, Pellerano S, Charbon E, Sebastiano F and Babaie M 2020 *IEEE Transactions on Circuits and Systems I: Regular Papers* **67** 5380
[25] Ryan C A, Johnson B R, Ristè D, Donovan B and Ohki T A 2017 *Rev. Sci. Instrum.* **88** 104703
[26] Koch J, Terri M Y, Gambetta J, *et al.* 2007 *Phys. Rev. A* **76** 042319
[27] Barends R, Kelly J, Megrant A, *et al.* 2013 *Phys. Rev. Lett.* **111** 080502
[28] Herrmann J, Hellings C, Lazar S, *et al.* 2022 arXiv: 2210.02513
[29] Li Z, Liu P, Zhao P, *et al.* 2023 *npj Quantum Information* **9** 111
[30] Das S and Suganthan P N 2010 *IEEE Transactions on Evolutionary Computation* **15** 4
[31] Motzoi F, Gambetta J M, Rebentrost P and Wilhelm F K 2009 *Phys. Rev. Lett.* **103** 110501
[32] Magesan E, Gambetta J M and Emerson J 2011 *Phys. Rev. Lett.* **106** 180504
[33] Magesan E, Gambetta J M and Emerson J 2012 *Phys. Rev. A* **85** 042311
[34] Barends R, Kelly J, Megrant A, *et al.* 2014 *Nature* **508** 500
[35] Kelly J, Barends R, Campbell B, *et al.* 2014 *Phys. Rev. Lett.* **112** 240504
[36] Kelly J, O'Malley P, Neeley M, Neven H and Martinis J M 2018 arXiv: 1803.03226